

## COMPARISON OF NUMERICAL METHODS FOR TERNARY FLUID FLOWS: IMMERSED BOUNDARY, LEVEL-SET, AND PHASE-FIELD METHODS

SEUNGGYU LEE<sup>1</sup>, DARAE JEONG<sup>1</sup>, YONGHO CHOI<sup>1</sup>, AND JUNSEOK KIM<sup>1,†</sup>

<sup>1</sup>DEPARTMENT OF MATHEMATICS, KOREA UNIVERSITY, SEOUL 136-713, KOREA

**ABSTRACT.** This paper reviews and compares three different methods for modeling incompressible and immiscible ternary fluid flows: the immersed boundary, level set, and phase-field methods. The immersed boundary method represents the moving interface by tracking the Lagrangian particles. In the level set method, an interface is defined implicitly by using the signed distance function, and its evolution is governed by a transport equation. In the phase-field method, the advective Cahn–Hilliard equation is used as the evolution equation, and its order parameter also implicitly defines an interface. Each method has its merits and demerits. We perform the several simulations under different conditions to examine the merits and demerits of each method. Based on the results, we determine the most suitable method depending on the specific modeling needs of different situations.

### 1. INTRODUCTION

A double emulsion, or compound droplet, is a specific case of a ternary fluid mixture. It has a smaller drop or drops inside a larger drop and has a high level of potential for many applications that use liquid membranes for selective mass transport, such as drug delivery and controlled drug release, because of its three phases: a small inner drop, the surrounding medium, and a third fluid [1]. However, modeling or simulating the interfaces of ternary fluid flows is a challenging problem since the diffusion phenomenon is more complex than two-component mixtures [2]. Figure 1 presents a schematic of the coaxial microcapillary fluidic device and the geometry of the double emulsion that it generates [3].

---

Received by the editors March 2 2016; Revised March 11 2016; Accepted in revised form March 11 2016; Published online March 24 2016.

2000 *Mathematics Subject Classification.* 76D05, 76M20, 76T30.

*Key words and phrases.* ternary fluid flows, continuum surface force, immersed boundary method, level set method, phase-field method, Navier–Stokes equation.

<sup>†</sup> Corresponding author. Email: [cfdkim@korea.ac.kr](mailto:cfdkim@korea.ac.kr); Tel: +82 2 3290 3077; Fax: +82 2 929 8562; <http://math.korea.ac.kr/~cfdkim>.

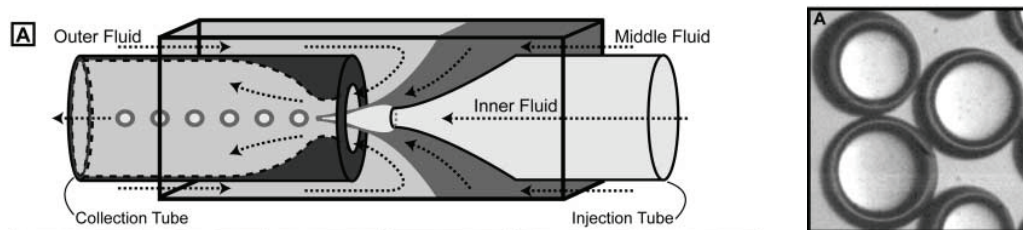


FIGURE 1. Schematic of the coaxial microcapillary fluidic device and the geometry of the double emulsion that is generated. The image is reprinted from [3]. Copyright ©Science 2005. Reprinted with permission. All rights reserved.

There are two major approaches to simulating multi-phase or multi-component flows to characterize moving interfaces: the interface tracking method and the interface capturing method. The interface tracking method uses computational mesh to track interfaces and a velocity field is generated by adjusting the position of nodes. Examples of the interface tracking method include the volume of fluid, front tracking, and immersed boundary method (IBM). In contrast, interface capturing methods implicitly define an interface by using the contours of particular scalar functions. Examples include the level set method (LSM) and phase-field method (PFM). In this paper, we review three methods, IBM, LSM, and PFM, to simulate ternary fluid flows with a double emulsion case and describe the basic techniques of each method in detail.

IBM was originally developed to model the blood flow in the heart by Peskin [4]; this method has been applied to various biological or industrial modeling problems. IBM has been used to research the hydrodynamics of a compound drop for application to leukocyte modeling [5, 6]. IBM has been applied not only to biological modeling problems as originally developed but also to fluid dynamics modeling problems [7, 8, 9]. The dynamics of a compound droplet in shear flow was researched in [10]. See the articles [11, 12, 13] to refer to the treatment of the multiple junction case with a foam model.

LSM uses a level set function to capture moving interfaces and has become popular in many disciplines since its development by Osher and Sethian in the 1980s [14]. More detailed reviews of classical LSM are given by [15, 17]. There have been developments to capture the fluid flow interfaces of ternary or even more phases by using LSM. Merriam et al. [18] represented each phase by using an individual level set function. The projection method, which uses only  $(n - 1)$ -level set functions to represent the interfaces of  $n$ -phases, was developed to resolve the triple junction problem by Smith et al. [19].

PFM is a popular method for modeling the dynamics of multi-phase fluids coupled with the Navier–Stokes equation [20]. It has a diffused interface with a finite but small width between distinct phases and characterizes physical quantities such as the density and viscosity by using an order parameter governed by the modified Cahn–Hilliard (CH) equation. The CH equation was first introduced by Cahn and Hilliard [21] to describe the initial stage of spinodal decomposition. It is often used to model interface dynamics, including surface minimization and sharp topological changes like pinch-off and phase separation. See [22] and the references

therein for detailed review of the method. The multi-component system was first generalized in the literature by de Fontaini [23] and Eyre studied its differences with the binary case and its dynamics [24]. Numerical studies of ternary CH systems have been vigorously pursued [25, 26, 27, 28, 29, 30].

The main goal of this paper is to review and compare three different methods. By comparing fundamental weakness and strength, it is expected to give an advice about a choice of the methods for the beginners in ternary fluid flows problem. Moreover, this paper could be helpful also to experts of this field developing a hybrid method as in the research of Hou et al.[31] by understanding unfamiliar methods to them.

This paper is organized as follows. In Section 2, we present the governing equations for IBM, LSM, and PFM. We summarize the formulas for the surface tension force in Section 3. In Section 4, we present the numerical method to solve the discrete Navier–Stokes equations and the respective equations for the interface. The numerical results are presented in Section 5. Finally, the conclusions are drawn in Section 6.

## 2. GOVERNING EQUATIONS AND INTERFACE REPRESENTATION

We consider incompressible and immiscible ternary fluids in a two-dimensional domain  $\Omega$  for simplicity. Its extension to a three-dimensional problem is straightforward. For more details, refer to [10] for IBM, [32, 33, 34] for on LSM, and [28, 35] for on PFM. The motion of fluid flows is generally described by the modified Navier–Stokes (NS) equations with the surface tension force:

$$\rho \left( \frac{\partial \mathbf{u}}{\partial t} + \mathbf{u} \cdot \nabla \mathbf{u} \right) = -\nabla p + \nabla \cdot [\eta(\nabla \mathbf{u} + \nabla \mathbf{u}^T)] + \mathbf{SF} \text{ in } \Omega, \quad (2.1)$$

$$\nabla \cdot \mathbf{u} = 0 \text{ in } \Omega, \quad (2.2)$$

where  $\rho(\mathbf{x}, t)$  is the density,  $\mathbf{u}(\mathbf{x}, t) = (u(\mathbf{x}, t), v(\mathbf{x}, t))$  is the velocity,  $p(\mathbf{x}, t)$  is the pressure,  $\eta(\mathbf{x}, t)$  is the viscosity,  $\mathbf{x} = (x, y)$  is the Cartesian coordinate,  $t$  is the time variable, and  $\mathbf{SF}$  is the surface tension force density. We assumed that  $\rho$  and  $\eta$  are constant for simplicity. A schematic of the three-phase domain  $\Omega = \Omega_1 \cup \Omega_2 \cup \Omega_3$  is shown in Fig. 2.  $\Gamma_k$  represents the interface between the fluids  $k$  and  $k + 1$ .

We can rewrite (2.1) and (2.2) by using dimensionless parameters as follows:

$$\frac{\partial \mathbf{u}}{\partial t} + \mathbf{u} \cdot \nabla \mathbf{u} = -\nabla p + \frac{1}{Re} \Delta \mathbf{u} + \mathbf{SF} \text{ in } \Omega, \quad (2.3)$$

$$\nabla \cdot \mathbf{u} = 0 \text{ in } \Omega. \quad (2.4)$$

Here,  $Re = \rho U^* L^* / \eta$  is the Reynolds number. where  $U^*$  is the characteristic velocity, and  $L^*$  is the characteristic length

Now, we briefly describe how IBM, LSM, and PFM represent the interfaces of multi-phase fluids by using a Lagrangian variable, level set function, and phase-field function, respectively. The governing equations of the interface evolution are also introduced in each section.

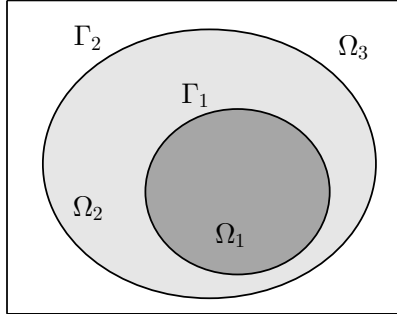


FIGURE 2. Schematic of a three-phase domain.

2.1. **IBM.** In IBM, the interfaces  $\Gamma_1$  and  $\Gamma_2$  are described by the Lagrangian variables  $\mathbf{X}_1(s_1, t)$  and  $\mathbf{X}_2(s_2, t)$ , respectively. Here,  $0 \leq s_k \leq L_k(t)$  and  $L_k(t)$  are the lengths of interfaces at time  $t$  for  $k = 1, 2$ . The evolution of the interface is governed by

$$\frac{\partial \mathbf{X}_k(s_k, t)}{\partial t} = \mathbf{U}_k(s_k, t), \quad (2.5)$$

$$\mathbf{U}_k(s_k, t) = \int_{\Omega} \mathbf{u}(\mathbf{x}, t) \delta^2(\mathbf{x} - \mathbf{X}_k(s_k, t)) d\mathbf{x}, \quad \text{for } k = 1, 2, \quad (2.6)$$

where  $\mathbf{U}_k(s_k, t)$  is the velocity of the Lagrangian variable  $\mathbf{x}_k(s_k, t)$ ,  $\mathbf{u}(\mathbf{x}, t)$  is the velocity field on a Cartesian grid,  $\delta^2(\mathbf{x})$  is the two-dimensional Dirac-delta function defined by the product of the one-dimensional Dirac-delta functions,  $\delta^2(\mathbf{x}) = \delta(x)\delta(y)$ . Figure 3 shows the Lagrangian variables representing interfaces on the domain  $\Omega$ .

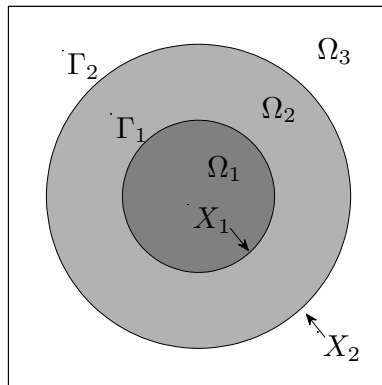


FIGURE 3. Lagrangian variables representing interfaces in the domain.

The principal advantage of IBM compared to the other two methods is that it can use a large number of interfacial marker points to handle the interface geometry for high accuracy. The major drawback is the difficulty of representing topological changes without additional work. Moreover, area conservation does not hold in general because the interfaces between each fluids move discretely [10].

**2.2. LSM.** In LSM, the interfaces of each two phases are defined implicitly with the level set functions  $\phi_k(\mathbf{x}, t)$ ,  $k = 1, 2$ . Here,  $\phi_1$  and  $\phi_2$  are the signed distances that satisfy  $|\nabla\phi_k| = 1$  from the interfaces  $\Gamma_1$  and  $\Gamma_2$ , respectively. Note that the values of  $\phi_k$  become zero at the interfaces, i.e., the zero contours of  $\phi_k$  represent the interfaces. Figure 4 shows the zero contour of the signed distance function and surface plots with zero contours. In addition, note that  $\phi_k$  has the opposite sign in each phase (see Fig. 4).

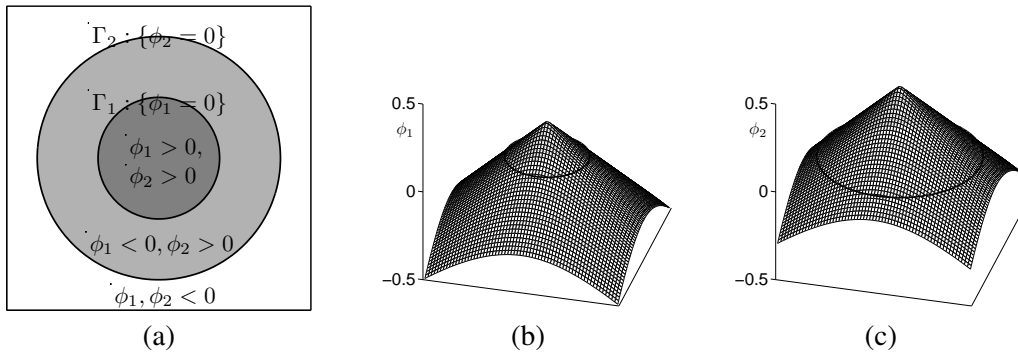


FIGURE 4. (a) Zero contours of the signed distance functions  $\phi_1$  and  $\phi_2$ , and surface plots with zero contours of (b)  $\phi_1$  and (c)  $\phi_2$ .

The evolution equation of  $\phi_k$  is governed by the transport equation:

$$(\phi_k)_t + \mathbf{u} \cdot \nabla \phi_k = 0. \quad (2.7)$$

During the process of interface evolution,  $\phi_k$  tends to deviate from the signed distance function. However, we maintained  $\phi_k$  as the signed distance function because the density and surface tension depend on  $\phi_k$  [36]. The reinitialization step makes  $\phi_k$  recover to the signed distance function without changing its zero contour and is given as follows:

$$\frac{\partial d_k}{\partial \tau}(\mathbf{x}, t) = S(\phi_k(\mathbf{x}, t))(1 - |\nabla d_k(\mathbf{x}, t)|), \quad (2.8)$$

$$d_k(\mathbf{x}, 0) = \phi_k(\mathbf{x}, t), \quad (2.9)$$

where  $\tau$  is the pseudo-time and  $S(\phi_k)$  is the sign function. In numerical implementations, we can use the smoothed sign function  $S_\beta(\phi_k) = \phi_k / \sqrt{\phi_k^2 + \beta^2}$  where  $\beta$  is one or two grid lengths.  $d_k(\mathbf{x}, \tau_s)$  replaces  $\phi_k(\mathbf{x}, t)$  after the function is solved up to the steady-state where  $\tau_s$  is the steady-state pseudo-time. A more detailed description is given in [15].

The advantages of LSM include a simple implementation, ability to automatically capture the merging and break-up of interfaces, and flexibility to describe the complex interface geometry. Whereas, the major disadvantage is the lack of mass (area) conservation and the hybrid methods have been proposed until nowadays to overcome this [16].

**2.3. PFM.** In PFM, the order parameters  $c_k(\mathbf{x}, t)$  are used, where  $k = 1, 2, 3$  which are measures of the relative composition or the volume fraction of the three components. The functions  $c_k$  are distributed continuously on thin interfacial layers and uniformly in the bulk phases. Here, the order parameter is defined by  $c_k \approx 1$  in one fluid and  $c_k \approx 0$  in the other fluid, while the interfaces  $\Gamma_k$  are defined by  $c_k = 0.5$ . The sharp fluid interfaces are replaced by thin (but nonzero) thickness transition regions. Figure 5 shows the numerical interfaces of the order parameters and surface plots with interfaces.

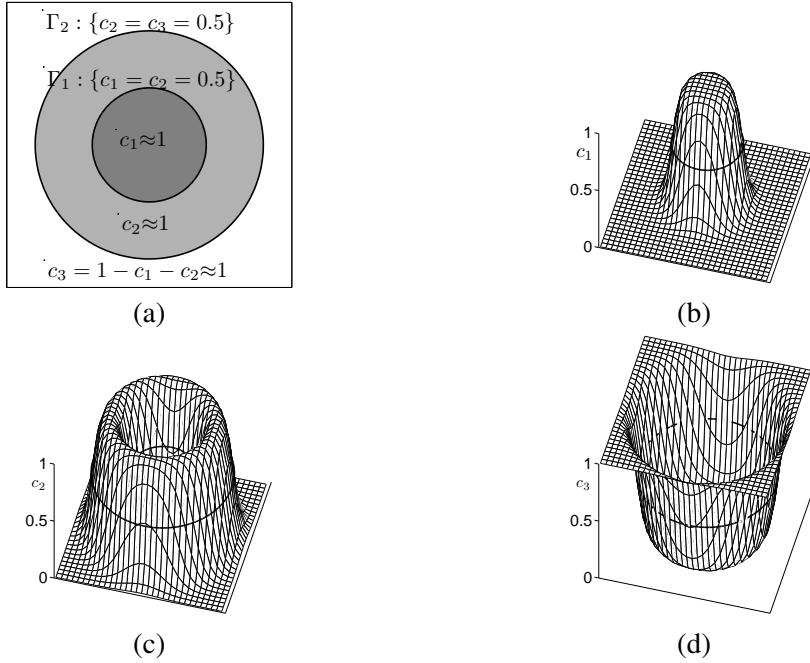


FIGURE 5. (a) Numerical interfaces of the order parameters  $c_1$  and  $c_2$ , and surface plots with the interfaces of (b)  $c_1$ , (c)  $c_2$ , and (d)  $c_3 = 1 - c_1 - c_2$ .

The evolution equations of the phase-field function  $\mathbf{c} = (c_1, c_2, c_3)$  are governed by the advective multi-component CH as follows:

$$\frac{\partial c_k}{\partial t} + \mathbf{u} \cdot \nabla c_k = \frac{1}{Pe} \Delta \mu_k, \quad k = 1, 2, 3 \quad (2.10)$$

$$\mu_k = \frac{\partial F(c_1, c_2, c_3)}{\partial c_k} - C \Delta c_k + \gamma(c_1, c_2, c_3), \quad (2.11)$$

where  $Pe$  is the Peclet number, defined by  $L^*U^*/(M\mu^*)$ ,  $M$  is the constant mobility,  $\mu^*$  is the characteristic value of the chemical potentials,  $\mu_k$  is the chemical potential,  $F(c_1, c_2, c_3) = 0.25 \sum_{k=1}^3 c_k^2(1 - c_k)^2$  is the bulk energy density,  $C$  is the Cahn number, defined by  $\epsilon^2/\mu^*$ ,  $\epsilon$  is the measure of the interface thickness and  $\gamma(c_1, c_2, c_3) = -\sum_{k=1}^3 \partial F / (3\partial c_k)$  is the Lagrangian multiplier which makes the sum of chemical potential  $\mu_k$  zero. See [37] for a detailed derivation of  $\gamma$ . Here, we only need to solve  $c_1$  and  $c_2$  because the sum of the mole fractions is unity ( $c_1 + c_2 + c_3 = 1$ ) from the definition of the order parameter. We can use the zero Neumann boundary condition for the CH systems:

$$\nabla c_k \cdot \mathbf{n} = \nabla \mu_k \cdot \mathbf{n} = 0 \text{ on } \partial\Omega, \quad (2.12)$$

where  $\mathbf{n}$  is the unit normal vector to  $\partial\Omega$ . The boundary condition (2.12) is natural and conserves the total mass in  $\Omega$ .

As shown in Fig. 6, the concentration field varies from 0.05 to 0.95 over a distance about  $\xi = 2\sqrt{2}\epsilon \tanh^{-1}(0.9)$  from the equilibrium profile  $c(x) = 0.5 + 0.5 \tanh(x/(\sqrt{2}\epsilon))$  in the infinite domain [38].

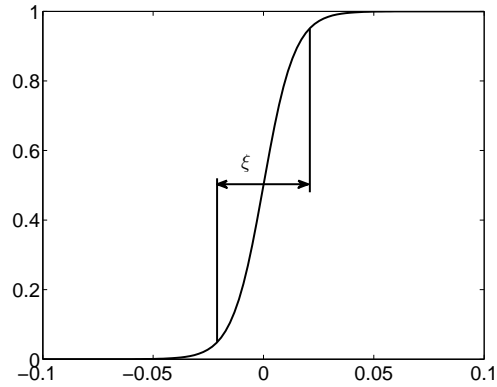


FIGURE 6. Phase transition of the equilibrium profile  $c(x) = 0.5 + 0.5 \tanh(x/(\sqrt{2}\epsilon))$ .

The advantages of LSM given above also apply PFM. Moreover, physical meanings of the order parameters can be applied to many physical phase states such as miscible, immiscible, and partially miscible. However, PFM needs a relatively large number of grid points near the interface because the phase-field function changes quickly near the interface. Moreover, it is important to choose appropriate  $\epsilon$  values for accurate calculations. An excessively large  $\epsilon$  can produce nonphysical solutions, whereas an excessively small  $\epsilon$  can cause numerical difficulties [39].

### 3. SURFACE TENSION FORCE

The singular surface tension force  $\mathbf{SF}$  is represented by the continuum surface force (CSF) model [40]:

$$\mathbf{SF} = -\frac{\sigma\kappa\delta_\Gamma\mathbf{n}}{We}, \quad (3.1)$$

where  $\kappa$  is the mean curvature of the interface and  $\delta_\Gamma$  is the surface delta function,  $We = \rho(U^*)^2 L^* / \sigma$  is the Weber number, and  $\sigma$  is the surface tension coefficient. Instead of  $\delta_\Gamma$ , a smoothed delta function is usually used to adapt the CSF framework to spread the interfacial force to the nearby grid points in numerical implementations.

We describe how to define the surface tension force for each method in the remainder of this section.

**3.1. IBM.** The surface tension force in IBM is given by

$$\mathbf{SF}(\mathbf{x}, t) = \sum_{k=1}^2 \int_{\Gamma_k} \frac{1}{We_k} \mathbf{F}_k(s_k, t) \delta^2(\mathbf{x} - \mathbf{X}_k(s_k, t)) ds, \quad (3.2)$$

$$\mathbf{F}_k(s_k, t) = \sigma_k \frac{\partial^2 \mathbf{X}_k(s_k, t)}{\partial s_k^2}, \quad (3.3)$$

where  $\mathbf{F}_k(s, t)$  is the boundary force defined for each particle of the  $k$ -th interface and  $We_k$  is the Weber number with the  $k$ -th interface's surface tension coefficient  $\sigma_k$ . The smoothed delta function  $\delta(x)$  is defined as [41] :

$$\delta(x) = \begin{cases} 0.125 \left( 3 - 2|x| + \sqrt{1 + 4|x| - 4x^2} \right), & \text{if } |x| \leq 1, \\ 0.125 \left( 5 - 2|x| - \sqrt{-7 + 12|x| - 4x^2} \right), & \text{if } 1 < |x| \leq 2, \\ 0, & \text{otherwise.} \end{cases} \quad (3.4)$$

We usually call (3.4) a four-point delta function. The schematics of the smoothed delta function  $\delta(x)$  and its two-dimensional version  $\delta^2(\mathbf{x}) = \delta(x)\delta(y)$  are shown in Figs. 7 (a) and (b), respectively.

Note that  $\partial^2 \mathbf{X}_k(s_k, t) / \partial s_k^2$  accounts for the interface curvature  $\kappa$ . Because the marker points of the moving interfaces and the grid points of the velocity field do not coincide directly, the interpolation is performed by using (3.4) to spread the surface tension force into the underlying grid points.

**3.2. LSM.** The surface tension force using the level set functions  $\phi_k(\mathbf{x}, t)$  is given by

$$\mathbf{SF}(\mathbf{x}, t) = -\sum_{k=1}^2 \frac{1}{We_{k,k+1}} \nabla \cdot \left( \frac{\nabla \phi_k}{|\nabla \phi_k|} \right) \delta_\alpha(\phi_k) \frac{\nabla \phi_k}{|\nabla \phi_k|}, \quad (3.5)$$

where  $We_{k,k+1}$  is the Weber number with the physical surface tension coefficient  $\sigma_{k,k+1}$  between the fluids  $k$  and  $k+1$ , which satisfies  $\sigma_{k,k+1} = \sigma_k + \sigma_{k+1}$  for the phase specific surface

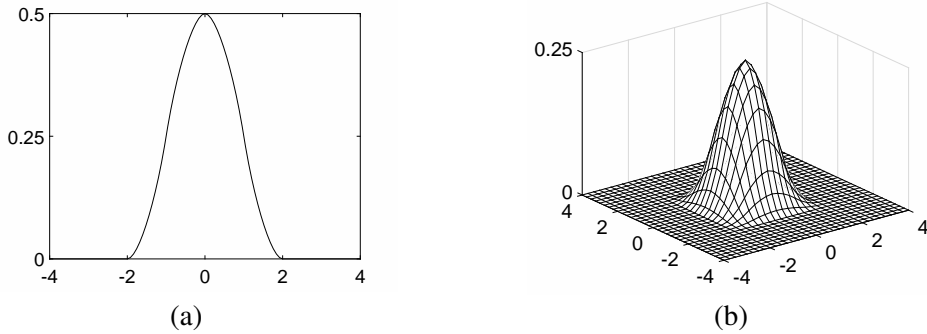


FIGURE 7. Schematics of (a) the smoothed delta function  $\delta(x)$  and (b) its two-dimensional version  $\delta^2(\mathbf{x}) = \delta(x)\delta(y)$ .

tension coefficient  $\sigma_k$  (see [19]). Recall that  $\sigma_{3,1}$  would not be defined in our compound droplet case. In addition, the smoothed delta function  $\delta_\alpha$  as follows [36] :

$$\delta_\alpha(\phi) = \begin{cases} \frac{1}{2\alpha} + \frac{1}{2\alpha} \cos\left(\frac{\pi\phi}{\alpha}\right), & \text{if } |\phi| \leq \alpha, \\ 0, & \text{otherwise.} \end{cases} \quad (3.6)$$

Note that the interface curvature  $\kappa$  is calculated by  $\nabla \cdot (\nabla\phi_k/|\nabla\phi_k|)$  and that the unit normal vector  $\mathbf{n}$  is represented by  $-\nabla\phi_k/|\nabla\phi_k|$ .

Here, we only consider the physical surface tension coefficient for  $k = 1, 2$  because our focus is on the compound droplet case. Meanwhile, the phase specific surface tension coefficient  $\sigma_k$  is uniquely defined as  $\sigma_1 = (\sigma_{12} - \sigma_{23} + \sigma_{13})/2$ ,  $\sigma_2 = (\sigma_{12} + \sigma_{23} - \sigma_{13})/2$ , and  $\sigma_3 = (-\sigma_{12} + \sigma_{23} + \sigma_{13})/2$  by the relation between physical surface tension coefficients.

**3.3. PFM.** The surface tension force using the phase-field functions  $c_k(\mathbf{x}, t)$  is written in the form

$$\mathbf{SF}(\mathbf{x}, t) = -\frac{\alpha\epsilon}{We_k} \nabla \cdot \left( \frac{\nabla c_k}{|\nabla c_k|} \right) |\nabla c_k| \nabla k_2, \quad (3.7)$$

where  $\alpha$  is the variable to match the surface tension of the sharpened interface model and satisfies

$$\int_{-\infty}^{\infty} \alpha\epsilon |\nabla c_k^{eq}(x, y)|^2 dx = 1. \quad (3.8)$$

Here,  $c_k^{eq}(x, y) = 0.5[1 + \tanh(x/(2\sqrt{2}\epsilon))]$  is an equilibrium profile in the infinite domain  $(-\infty, \infty) \times (-\infty, \infty)$  with  $c_3 \equiv 0$  [42]. Therefore, we get  $\alpha = 6\sqrt{2}$  from Eq. (3.8). Here, we only consider the case of  $k = 2$  because our focus is on the compound droplet case.

#### 4. NUMERICAL SOLUTION

In this section, we briefly describe the numerical solutions for the dimensionless NS equations (2.3) and (2.4), evolution equations (2.5) and (2.6), (2.7), (2.10) and (2.11) for IBM, LSM, and PFM in the two-dimensional domain.

**4.1. Discretization.** We first discretize the computational domain  $\Omega = (a, b) \times (c, d)$  before solving the governing equations numerically. In Cartesian geometry, we consider  $h = (b - a)/N_x = (d - c)/N_y$  to be a uniform spatial step size where  $N_x$  and  $N_y$  are the numbers of cells in the  $x$ - and  $y$ -directions, respectively. This implies that  $\mathbf{x}_{ij} = (x_i, y_j)$  is located at the cell center where  $x_i = a + (i - 0.5)h$  and  $y_j = c + (j - 0.5)h$  for  $i = 1, \dots, N_x$  and  $j = 1, \dots, N_y$ . We denote  $u(x_i, y_j, n\Delta t)$  as  $u_{ij}^n$  where  $\Delta t$  is a temporal step size in the discretized domain. The discrete gradient operator  $\nabla_h$  is defined with the forward difference as  $\nabla_h \phi_{ij}^n = \left( (\phi_{i+1,j}^n - \phi_{ij}^n)/h, (\phi_{i,j+1}^n - \phi_{ij}^n)/h \right)$ . The discrete Laplacian operator  $\Delta_h$  is defined with the central difference as  $\Delta_h \phi_{ij}^n = (\phi_{i+1,j}^n + \phi_{i-1,j}^n + \phi_{i,j+1}^n + \phi_{i,j-1}^n - 4\phi_{ij}^n)/h^2$  in Cartesian coordinates. We can use a staggered marker-and-cell (MAC) mesh that stores the pressure value  $p_{ij}$  at a cell center and the velocity values  $u_{i+1/2,j}$  and  $v_{i,j+1/2}$  at the cell edges in the  $x$ - and  $y$ -directions, respectively (see Fig. 8). The level set function, phase-field function, and surface tension values  $\phi_{k,ij}^n$ ,  $c_{k,ij}^n$ , and  $\mathbf{SF}_{ij}^n$  are also stored in the cell centers as pressure values.

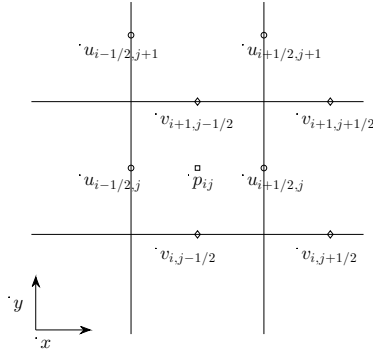


FIGURE 8. MAC mesh that stores pressure value  $p_{ij}$  at a cell center and the velocity values  $u_{i+1/2,j}$  and  $v_{i,j+1/2}$  at the cell edges in the  $x$ - and  $y$ -directions, respectively.

In contrast, IBM uses a set of Lagrangian points, whose coordinates do not depend on the MAC mesh grid, to discretize the immersed boundary. There are  $M_1$  Lagrangian points  $\mathbf{X}_{1,l}^n = (X_{1,l}^n, Y_{1,l}^n)$  for  $l = 1, \dots, M_1$  to represent the inner droplet boundary and  $M_2$  Lagrangian points  $\mathbf{X}_{2,l}^n = (X_{2,l}^n, Y_{2,l}^n)$  for  $l = 1, \dots, M_2$  to represent the outer droplet boundary.

**4.2. Fluid solution.** The temporal discretization of (2.3) and (2.4) is as follows:

$$\frac{\mathbf{u}^{n+1} - \mathbf{u}^n}{\Delta t} = -\nabla_h p^{n+1} + \frac{1}{Re} \Delta_h \mathbf{u}^n + \mathbf{SF}^n - (\mathbf{u} \cdot \nabla_h \mathbf{u})^n, \quad (4.1)$$

$$\nabla_h \cdot \mathbf{u}^{n+1} = 0. \quad (4.2)$$

Here, the discrete surface tension force  $\mathbf{SF}^n$  is calculated from the variable  $\mathbf{X}^n$ ,  $\phi_k^n$ , or  $c_k^n$ . These represent the interfaces for each method, as discussed in the previous section 4.3. At each time step, (4.1) and (4.2) are solved to find  $\mathbf{u}^{n+1}$  and  $p^{n+1}$  from the given  $\mathbf{u}^n$ . We can apply the projection method, which was developed by Chorin [43]. Here, we present the outline of the main procedures of the method.

First, we consider the intermediate velocity  $\tilde{\mathbf{u}}$  and split the discrete equation (4.1) as follows:

$$\frac{\tilde{\mathbf{u}} - \mathbf{u}^n}{\Delta t} = \frac{1}{Re} \Delta_h \mathbf{u}^n + \mathbf{SF}^n - (\mathbf{u} \cdot \nabla_h \mathbf{u})^n, \quad (4.3)$$

$$\frac{\mathbf{u}^{n+1} - \tilde{\mathbf{u}}}{\Delta t} = -\nabla_h p^{n+1}. \quad (4.4)$$

By applying  $\nabla_h$  to both sides of (4.4) and the divergence free condition (4.2), we get the discrete Poisson equation for the pressure field:

$$\Delta_h p^{n+1} = \frac{1}{\Delta t} (\nabla_h \cdot \tilde{\mathbf{u}}). \quad (4.5)$$

We can solve (4.5) by using a multigrid method-specifically, V-cycles with a Gauss–Seidel relaxation.

In summary, we first update the intermediate velocity  $\tilde{\mathbf{u}}$  from (4.3). Next, we update the pressure field by solving (4.5). Finally, the velocity  $\mathbf{u}^{n+1}$  is calculated from (4.4).

**4.3. Surface tension force.** In this section, we present how to derive the discrete surface tension forces by using interface variables for each method. We store values of the force at cell-centers as the pressure values, i.e.,  $\mathbf{SF}_{ij}^n$  is defined in this section. However, the interpolated values  $(SF_{i+\frac{1}{2},j}^x, SF_{i,j+\frac{1}{2}}^y)$  at the cell-edges are used in the fluid equations (4.3) and (4.4) to match the stencils of the velocities.

**4.3.1. IBM.** By discretizing (3.2) and (3.3), we get the discrete surface tension force for IBM as below:

$$\mathbf{SF}_{ij}^n = \sum_{k=1}^2 \sum_{l=1}^{M_k} \frac{1}{We_k} \mathbf{F}_{k,l}^n \delta^2(\mathbf{x}_{ij} - \mathbf{X}_{k,l}^n) \Delta s_{k,l}, \quad (4.6)$$

$$\mathbf{F}_{k,l}^n = \sigma_k \left( \frac{\mathbf{X}_{k,l+1}^n - \mathbf{X}_{k,l}^n}{\Delta s_{k,l}} - \frac{\mathbf{X}_{k,l}^n - \mathbf{X}_{k,l-1}^n}{\Delta s_{k,l-1}} \right) \Big/ \frac{\Delta s_{k,l} + \Delta s_{k,l-1}}{2}, \quad (4.7)$$

where  $\Delta s_{k,l} = s_{k,l+1} - s_{k,l}$  is a line segment of each interface. Note that (4.7) is a multiple of the mean curvature and the normal vector at  $\mathbf{X}_{k,l}^n$ . Refer to [44] for a more detailed description and calculation of (4.7).

**4.3.2. LSM.** In LSM, the discrete surface tension force is derived from (3.5), and the force is given as

$$\mathbf{SF}_{ij}^n = -\sum_{k=1}^2 \frac{1}{We_{k,k+1}} \nabla_h \cdot \left( \frac{\nabla_h \phi_{k,ij}^n}{|\nabla_h \phi_{k,ij}^n|} \right) \delta_\alpha(\phi_{k,ij}^n) \frac{\nabla_h \phi_{k,ij}^n}{|\nabla_h \phi_{k,ij}^n|}. \quad (4.8)$$

Note that  $\alpha$  is usually taken as  $h$  or  $2h$ . Here, we select  $2h$ .

4.3.3. *PFM*. With PFM, the discrete surface tension force can be derived similarly to the LSM case. The force is formulated as follows:

$$\mathbf{SF}_{ij}^n = -\frac{6\sqrt{2}\epsilon}{We_2}\nabla_h \cdot \left( \frac{\nabla_h c_{2,ij}^n}{|\nabla_h c_{2,ij}^n|} \right) |\nabla_h c_{2,ij}^n| \nabla_h c_{2,ij}^n. \quad (4.9)$$

Because the interfaces are already diffused when using PFM, a delta function is not required to represent the surface tension force in (4.9).

4.4. **Governing equations of interfaces.** In this section, we discretize the governing equations of interfaces for each method and present their numerical solutions.

4.4.1. *IBM*. By using the updated fluid velocity  $\mathbf{u}^{n+1}$  in (4.3) and (4.4), we can evaluate the immersed boundary velocity  $\mathbf{U}^{n+1}$  and new boundary position  $\mathbf{X}^{n+1}$  according to the following equations:

$$\mathbf{U}_{k,l}^{n+1} = \sum_{i=1}^{N_x} \sum_{j=1}^{N_y} \mathbf{u}_{ij}^{n+1} \delta^2(\mathbf{x}_{ijk} - \mathbf{X}_{k,l}^{n+1} h^2), \quad (4.10)$$

$$\mathbf{X}_{k,l}^{n+1} = \mathbf{X}_{k,l}^n + \Delta t \mathbf{U}_{k,l}^{n+1}, \quad (4.11)$$

where  $k = 1, 2$  and  $l = 1, \dots, M_k$ . We can also apply the algorithms introduced by [44] and [45] for the high-quality distribution of the interface points and the area conservation property, respectively. See each reference for detailed descriptions of the properties.

4.4.2. *LSM*. The numerical solution of the evolution equation (2.7) is derived from the following discrete transport equation:

$$\frac{\phi_{k,ij}^{n+1} - \phi_{k,ij}^n}{\Delta t} = -\frac{u_{i+\frac{1}{2},j}^n (\phi_{k,i+1,j}^n - \phi_{k,ij}^n) + u_{i-\frac{1}{2},j}^n (\phi_{k,ij}^n - \phi_{k,i-1,j}^n)}{2h} - \frac{v_{i,j+\frac{1}{2}}^n (\phi_{k,i,j+1}^n - \phi_{k,ij}^n) + v_{i,j-\frac{1}{2}}^n (\phi_{k,ij}^n - \phi_{k,i,j-1}^n)}{2h}. \quad (4.12)$$

It is a very basic numerical solver and more accurate, stable, and conservative numerical methods such as a WENO-type difference and Godunov's scheme can be founded in [15]. Next, the discrete equations of the reinitialized steps (2.8) and (2.9) are given as

$$\tilde{d}_{k,ij} = d_{k,ij} + \Delta\tau \frac{\phi_{k,ij}^n}{\sqrt{(\phi_{k,ij}^n)^2 + \beta^2}} \left( 1 - \sqrt{(D_x d_{k,ij})^2 + (D_y d_{k,ij})^2} \right) \quad (4.13)$$

where the initial condition of  $d_{k,ij}$  is given as  $\phi_{k,ij}^n$ . The operators  $D_x$  and  $D_y$  are discrete differentiations in the WENO sense [36, 46] with respect to  $x$  and  $y$ , respectively. After a few iterations, we can update  $\phi_{k,ij}^n$  as the result of the final  $\tilde{d}_{k,ij}$ .

4.4.3. *PFM*. To discretize the CH equation, we consider the nonlinear splitting scheme over time. If the variable Lagrangian multiplier  $\gamma(c_1, c_2, c_3)$  is determined by  $c_1^n$ ,  $c_2^n$ , and  $c_3^n$ , i.e.,  $\gamma$  is treated explicitly, the solutions at the time level  $n + 1$  have no relation to each other. This implies that the ternary component CH system can be solved in a decoupled manner. Therefore, we can discretize (2.10) and (2.11) for  $k = 1, 2$  as follows:

$$\frac{c_{k,ij}^{n+1} - c_{k,ij}^n}{\Delta t} = \frac{1}{Pe} \Delta_h \mu_{k,ij}^{n+1} + \Delta_h (\gamma(c_{1,ij}^n, c_{2,ij}^n, c_{3,ij}^n) - 0.25c_{k,ij}^n) - \frac{u_{i+\frac{1}{2},j}^n (c_{k,i+1,j}^n - c_{k,ij}^n) + u_{i-\frac{1}{2},j}^n (c_{k,ij}^n - c_{k,i-1,j}^n)}{2h} - \frac{v_{i,j+\frac{1}{2}}^n (c_{k,i,j+1}^n - c_{k,ij}^n) + v_{i,j-\frac{1}{2}}^n (c_{k,ij}^n - c_{k,i,j-1}^n)}{2h}, \quad (4.14)$$

$$\mu_{k,ij}^{n+1} = f(c_{1,ij}^{n+1}, c_{2,ij}^{n+1}, c_{3,ij}^{n+1}) + 0.25c_{k,ij}^{n+1} - C \Delta_h c_{k,ij}^{n+1}. \quad (4.15)$$

This means that we can solve the ternary CH system by solving the binary CH equation twice. A nonlinear multigrid method can be used to solve (4.14) and (4.15). A detailed description is given by [47].

## 5. NUMERICAL EXPERIMENTS

Before performing numerical experiments, we note that a relation between the  $\epsilon$  value and the width of the transition layer for PFM. As mentioned in section 2.3, the equilibrium state of the concentration has a tangent hyperbolic profile. If we want to set  $\epsilon$  value to be about  $m$  grid points, the value is set as  $\epsilon_m = hm/4\sqrt{2} \tanh^{-1}(0.9)$  [48, 49]. Unless otherwise specified, we use  $\epsilon = \epsilon_4$ .

5.1. **Pressure difference.** The pressure gradient and surface tension force are balanced in the absence of viscous, gravitational, and other external forces. The pressure difference can be expressed by  $[p]_\Gamma = \sigma/R$  with Laplace's formula for a spherical liquid surrounded by an ambient fluid in a two-dimensional space, where  $R$  is the radius of the droplet. Therefore, the pressure jump of the compound droplet is defined by

$$[p]_\Gamma = [p]_{\Gamma_1} + [p]_{\Gamma_2} = \frac{\sigma_1}{R_1} + \frac{\sigma_2}{R_2}. \quad (5.1)$$

Here, circular droplets with  $R_1 = 0.5$  and  $R_2 = 1$  were taken as the initial conditions, and  $\sigma_1 = \sigma_2 = 1$  was used. Our numerical simulation was in the domain  $(0, 3) \times (0, 3)$  with the uniform grids  $h = 1/2^n$  for  $n = 5, 6, 7, 8$  and  $9$  for one time step. Table 1 lists the convergence of the pressure jump for each method between the ambient fluids and inner droplets as we refined the mesh size. Figures 9(b) and (c) show the pressure field on the  $xy$ -plane and along the line  $y = 1.5$ , respectively, for the compound droplets.

TABLE 1. Numerical pressure jump between the ambient fluids and inner droplet as the mesh size was refined for each method. The theoretical pressure jump was 3.

Mesh size ( $h$ )	Method	1/32	1/64	1/128	1/256
	LSM	3.0350	3.0216	3.0097	3.0066
$[p]_{\Gamma_1} + [p]_{\Gamma_2}$	PFM	2.5435	2.8875	2.9728	2.9854
	IBM	3.0027	3.0015	3.0017	3.0018

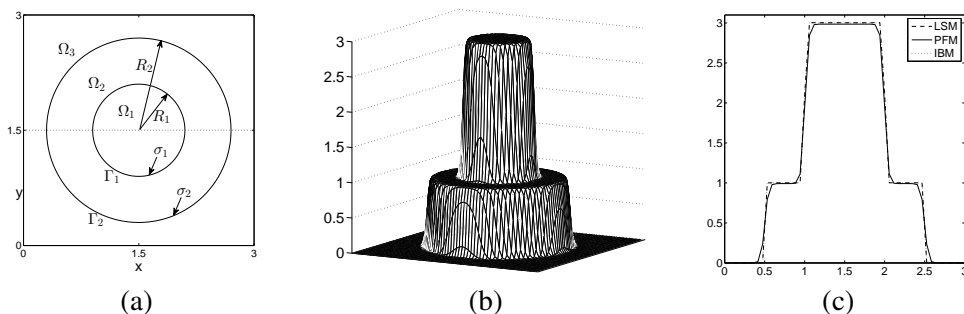


FIGURE 9. (a) Schematic illustration of a drop-in-drop surrounded by ambient fluid. (b) Pressure field for compound drop. (c) Slice of the pressure field at  $y = 1.5$  (dotted line in (a)) for each method.

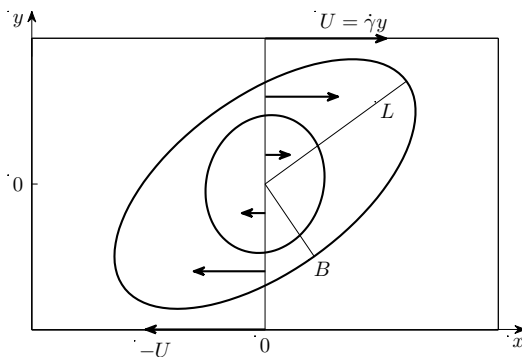


FIGURE 10. Schematic of a compound drop in the ambient fluid under a simple shear flow.

**5.2. Deformation of compound droplet under shear flow.** The imposed flow was a simple shear flow given by  $U = \dot{\gamma}y$  and  $v = 0$ , where  $\dot{\gamma}$  is the shear rate. Figure 10 presents a schematic of a compound drop in the ambient fluid under a simple shear flow.

We first introduce the Taylor deformation number  $D$ , defined as  $D = (L - B)/(L + B)$ , where  $L$  and  $B$  are the major and minor semiaxes of the droplet (See Fig. 10).  $D$  is usually used to measure the magnitude of the droplet deformation.

We confirm the effect of parameters such as the numbers of Lagrangian particles  $M_1$  and  $M_2$  in IBM, the number of repetitions of the reinitialization process in LSM, and  $Pe$  in PFM. The simulations are performed on a squared domain  $\Omega_h = (-2, 2) \times (-2, 2)$  with a  $128 \times 128$  meshgrid for 12500 iterations unless otherwise stated. The radii of the inner and outer droplets are  $R_1 = 0.5$  and  $R_2 = 1$ , respectively. We used the parameters  $\Delta t = 0.1h^2 Re$ ,  $Pe = 1$ ,  $We = 0.2$ , and  $\dot{\gamma} = 0.5$ , i.e., the velocity on the top of the domain is 1.

Figure 11 represents the shapes of the compound droplet with different numbers of immersed boundary points with  $64 \times 64$  meshgrid. The values in the legend mean initial distances of each Lagrangian particle, for example, about 4 particles are in the one mesh grid of the  $4h$  case. For each case,  $(M_1, M_2)$  are  $(101, 51)$ ,  $(51, 26)$ , and  $(26, 13)$  from top to bottom. It is convergent enough when there are at least one particle in one mesh grid as shown in the Fig. 11 and we will set the distance between each particle as about  $h/4$ .

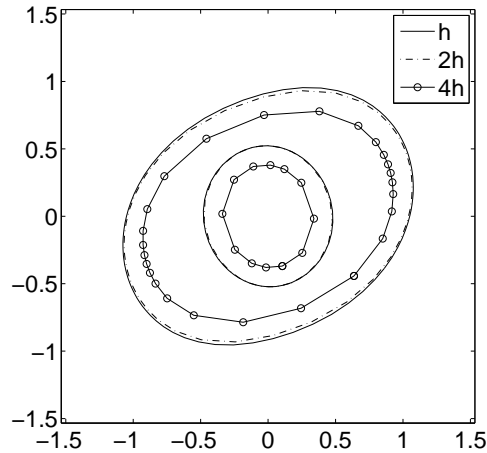


FIGURE 11. Shapes of the compound droplet with different number of immersed boundary points. The values in the legend mean initial distances of each Lagrangian particle.

We also compare the effect of  $n_\tau$  which is the number of repetition of reinitialization process. Figure 12 shows deformed shape of the compound droplet using the contour line at  $-2h$ ,  $0$ , and  $2h$  level, respectively. As shown in Fig. 12, the results with  $n_\tau = 0$  which mean that the reinitialization process has not taken place, have the difference with the numerical results when  $n_\tau = 1$  or  $5$ . The result is compatible with the suggestion, in the reference [36].

Before checking the effect of  $Pe$ , we first confirm that the choice of  $\epsilon_4$  is suitable enough. In Fig. 13, changes of deformation number  $D$  is presented varying time until  $T = 0.2941$ . The result shows that  $\epsilon_4$  and  $\epsilon_6$  cases have a better consistency with LSM and IBM than  $\epsilon_2$ .

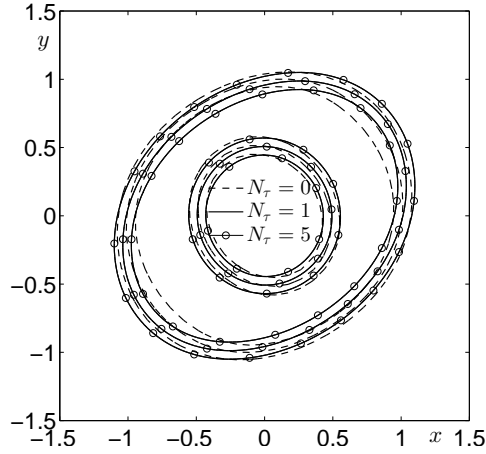


FIGURE 12. Shapes of the compound droplet with different number of repetition of reinitialization process.

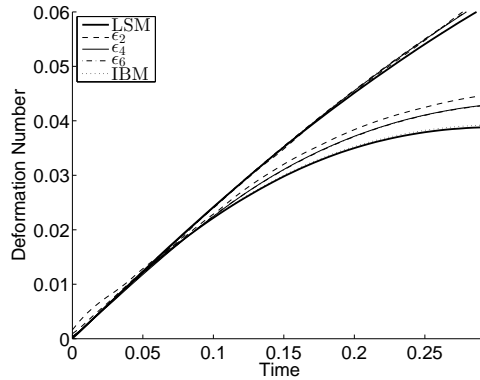


FIGURE 13. Changes of deformation number  $D$  is presented varying time until  $T = 0.2941$ .

Next, the simulations are performed to compare the effect of  $Pe$  in PFM. Figure 14 represents the deformed shapes of compound droplet with different  $Pe$  values. The top and bottom rows represent contour lines at 0.1, 0.5, and 0.9 levels of  $\phi_1$  and  $\phi_2$ , respectively. The  $Pe$  values are  $0.01/\epsilon$ ,  $1/\epsilon$ , and  $100/\epsilon$  in Fig. 14(a), (b), and (c), respectively. The result shows that degree of deformation could be too tenuous in the smallest  $Pe$  case (Fig. 14(a)) and thickness of the contour lines is not uniform in the biggest  $Pe$  case (Fig. 14(c)). Moreover, we compare shapes of compound droplets using LSM and PFM with different  $Pe$  values in Fig. 15. The results shows that the case using  $Pe = 1/\epsilon$  is the most consistent with LSM case. Therefore, We use  $Pe = 1/\epsilon$  in the later simulations unless otherwise stated.

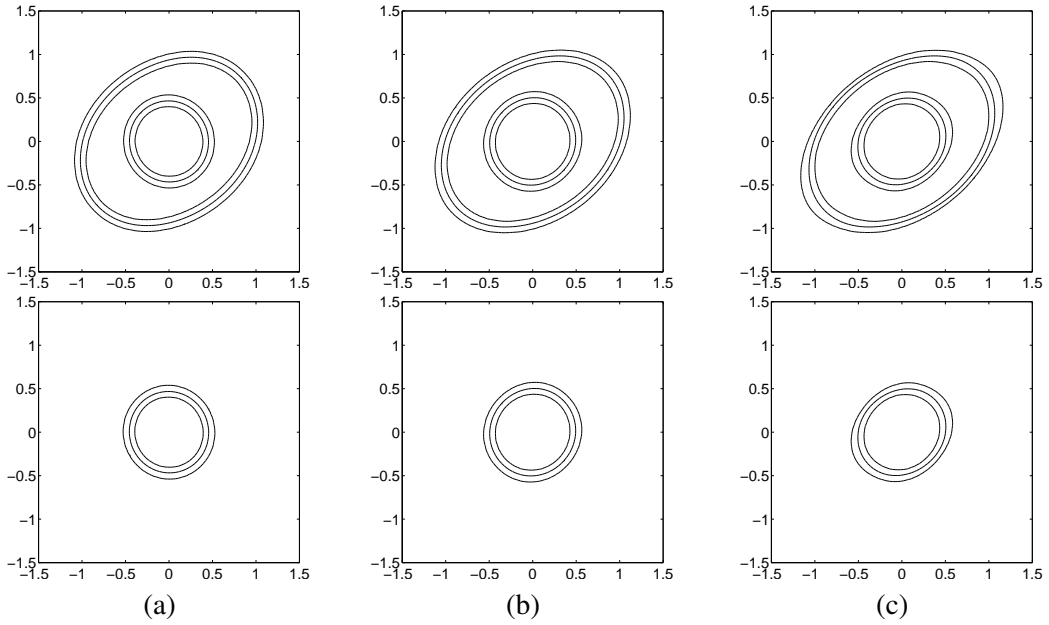


FIGURE 14. Shapes of compound droplet with different  $Pe$  values. The top and bottom rows represent contour lines at 0.1, 0.5, and 0.9 levels of  $\phi_1$  and  $\phi_2$ , respectively. The  $Pe$  values are (a)  $0.01/\epsilon$ , (b)  $1/\epsilon$ , and (c)  $100/\epsilon$ , respectively.

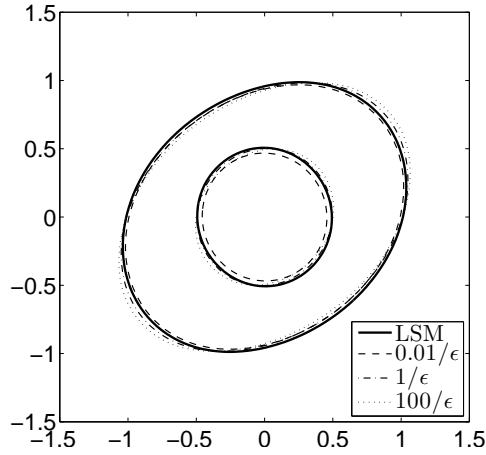


FIGURE 15. shapes of compound droplets using LSM and PFM with different  $Pe$  values.

### 5.3. Comparison with each method in specific cases.

5.3.1. *Multiple compound droplets case.* We perform the simulations of specific cases which are suitable to distinguish advantages and disadvantages for each method.

At first, the multiple compound droplets case like in the right side of Fig. 1 is chosen. We only consider two couples of emulsion for simplicity. The initial radii are  $R_1 = 0.5$  and  $R_2 = 1$  for each emulsion whose centers are located at  $(-0.74, -0.74)$  and  $(0.74, 0.74)$  on  $(-2, 2) \times (-2, 2)$ . The other parameters, except  $\dot{\gamma} = 0$ , have same values used in the simulations of section 5.2. If there is no flow outside of the droplets, emulsions do not collide or merge each other even though their distance is comparatively near in vivo.

Figure 16 represents the shapes of droplets at initial condition and at  $T = 0.1221$  solved by IBM, LSM, and PFM. The result shows that only IBM maintains the topological phase. It implies that IBM is the best in three methods when the densely distributed compound droplets are stabilized, or prevented the coalescence between droplets by employing surfactants. On the other hand, LSM or PFM is recommended to model the merged droplets without surfactants.

5.3.2. *Different radius of smaller droplet.* The coalescence can be happened between not only different emulsions, but also between an inner droplet and an outer droplet in one emulsion. Here, we consider another specific cases with different radii of smaller droplets to check whether each method can be treated such conditions well or not. We fix  $R_1 = 0.5$ ,  $Re = 1$ ,  $We = 0.1$ ,  $\dot{\gamma} = 0.5$ ,  $\Omega = (-2, 2) \times (-2, 2)$ ,  $\Delta t = 0.1h^2Re$  and  $T = 22500\Delta t$ .

Figure 17 represents the shapes of droplets at  $T$  using each method with different  $R_2$ . The emulsions have the same shape using any methods in a shear flow in Fig. 17 (a)  $R_2 = 0.7$ ; however, the inner droplet whose initial radius  $R_2$  is 0.8 is broken when only PFM is implemented as shown in Fig. 17 (b). The brokenness stems from a numerical error when interfaces of outer and inner droplets are too close since PFM uses a diffused-interface. From the result, we suggest that applying IBM or LSM might draw a better result rather than using PFM when sizes of outer and inner droplets in an emulsion are too similar to avoid merging each other.

5.3.3. *Mass conservation.* To compare mass conservation property in each method, we perform the simulation under the condition with a strong surface tension. The initial compound droplets, whose radii are  $R_1 = 0.5$  and  $R_2 = 1$ , are located at the center of the domain  $\Omega = (-2, 2) \times (-2, 2)$ . We choose  $We = 0.001$  and other parameters are same as the simulation in section 5.3.1.

Figure 18 represents the shapes of the droplets (a) at  $T = 0.4900$  using IBM, (b) at  $T = 2.9591$  using LSM, and (c) at  $T = 2.9591$  using PFM (dotted line) with the initial condition (solid line). Except PFM, the mass of droplets does not conserve and their area shrinks after several iterations even though there are no external force without surface tension force. Otherwise, the droplets solving PFM conserves its shape during longer or same temporal evolution than other methods. Therefore, using PFM is recommended when the simulation is performed with a strong surface tension from our result.

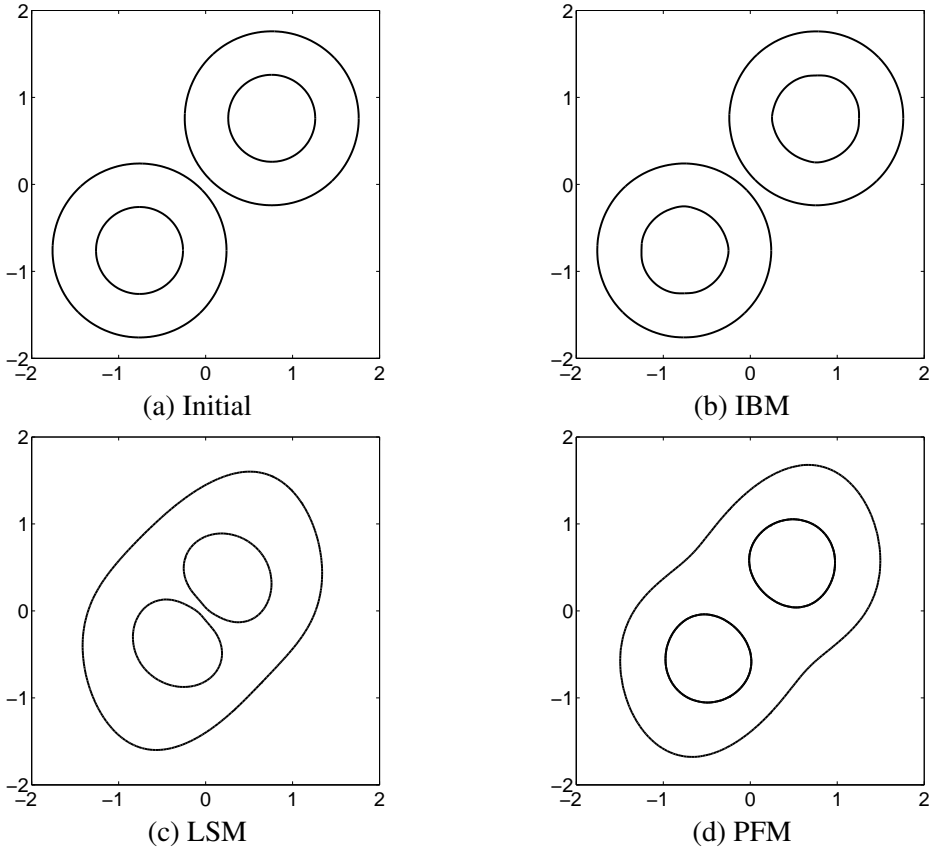


FIGURE 16. Shapes of droplets at (a) initial condition and at  $T = 0.1221$  solved by (b) IBM, (c) LSM, and (d) PFM.

5.3.4. *Different shear rate.* We checked the suitable or recommended cases using IBM or PFM by previous simulations. In this section, we examine the merits of using LSM rather than other two methods. Clearly, LSM has a better performance than IBM when there is any topological changes for droplets. Furthermore, it could be confirmed that LSM has an advantage over PFM of choosing compatible parameter values.

The initial radii, computational domain, and other parameters except the Peclet number  $Pe$ , the final time  $T$  and shear rate  $\dot{\gamma}$  are same as the simulation in section 5.3.1. The simulations with different  $\dot{\gamma} = 0.5$  and  $5$  are performed with  $Pe = 0.1/\epsilon$  until  $T = 0.2941$ . In Fig. 19, the changes of the deformation number varying time for LSM, PFM, and IBM (upper row) and the shapes of droplets at time  $T$  (lower row) are shown. As shown in Fig. 19, the evolution of droplet shapes and deformation numbers are distinct with different shear rate. To resolve this phenomenon,  $Pe$  should be differently chosen for different conditions, i.e., choosing suitable  $Pe$  is quite important in PFM. However, LSM does not have this restriction and is independent

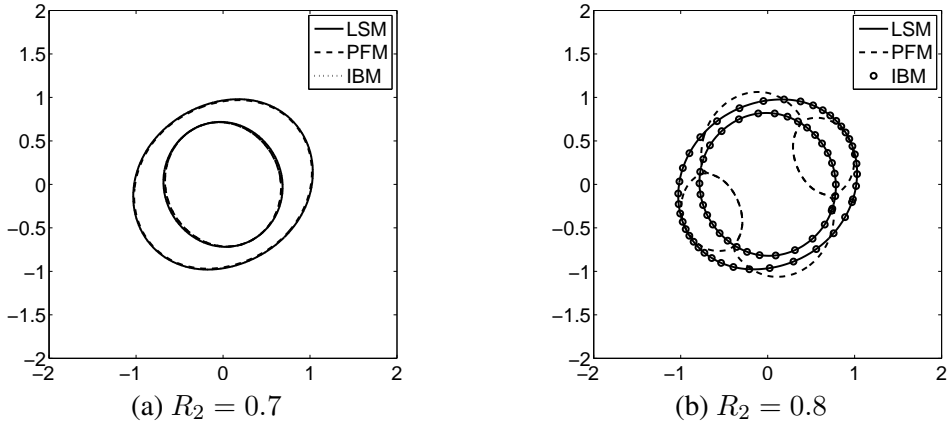


FIGURE 17. Shapes of droplets at  $T$  using each method with (a)  $R_2 = 0.7$  and (b)  $R_2 = 0.8$ .

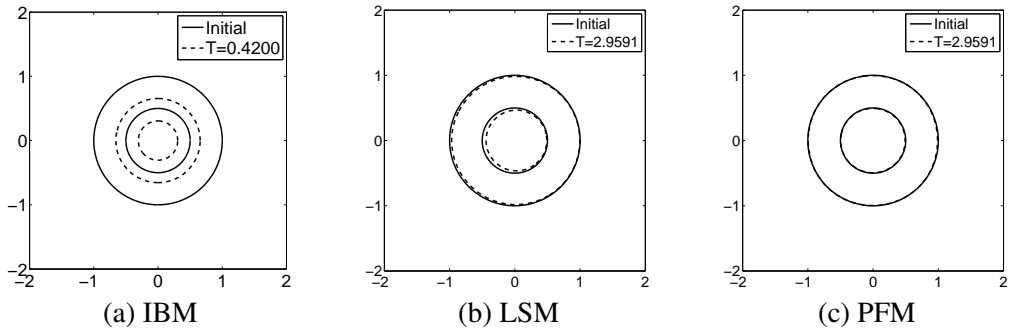


FIGURE 18. Shapes of the droplets (a) at  $T = 0.4200$  using IBM, (b) at  $T = 2.9591$  using LSM, and (c) at  $T = 2.9591$  using PFM (dotted line) with the initial condition (solid line).

on this choice problem. We suggest that LSM is better method than other two methods when comparison of different shear rate conditions is required.

## 6. CONCLUSION

The main goal of this paper was to review and compare three different methods such as immersed boundary, level set, and phase-field methods for incompressible, immiscible ternary fluid flows. We performed the simulations to investigate advantages and disadvantages of each method. Immersed boundary method was good for defining multiple droplets closely located each other and prevented from the coalescence. However, it was difficult to model topological transition phenomena. Level set method can deal with merging and pinch-off of interfaces, however it suffered from mass conservation. Phase-field method had a good property of mass

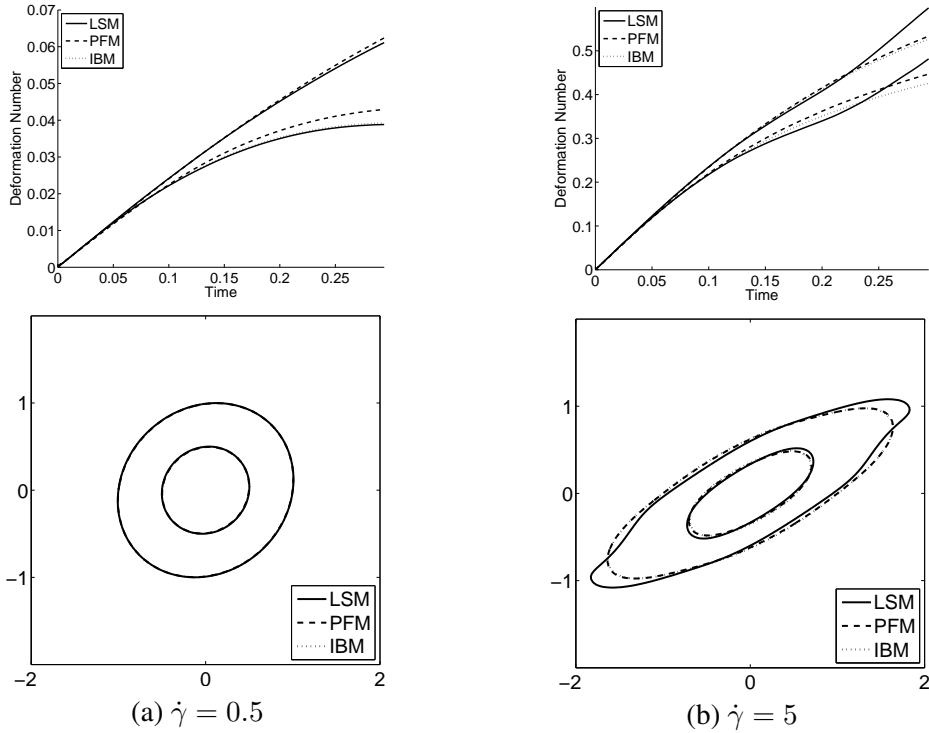


FIGURE 19. Changes of the deformation number varying time for LSM, PFM, and IBM (upper row) and shapes of droplets at time  $T$  (lower row)

conservation, however it had to choose an appropriate relaxation parameter such as mobility. Therefore, depending on one's need for modeling, we chose the most suitable method.

#### ACKNOWLEDGMENT

The corresponding author (J.S. Kim) was supported by the National Research Foundation of Korea (NRF) grant funded by the Korea government (MSIP) (NRF-2014R1A2A2A01003683).

#### REFERENCES

- [1] J.M. Park and P.D. Anderson, *A ternary model for double-emulsion formation in a capillary microfluidic device*, *Lab Chip*, **12**(15) (2012), 2672–2677.
- [2] L. Szalmás, *Viscous velocity, diffusion and thermal slip coefficients for ternary gas mixtures*, *Euro. J. Mech. B-Fluid.*, **53** (2015), 264–271.
- [3] A.S. Utada, E. Lorenceau, D.R. Link, P.D. Kaplan, and H.A. Stone, *Weitz DA. Monodisperse double emulsions generated from a microcapillary device*, *Science*, **308**(5721) (2005), 537–541.

- [4] C.S. Peskin, *Numerical analysis of blood flow in the heart*, J. Comput. Phys., **25**(3) (1977), 220–252.
- [5] H.C. Kan, H.S. Udaykumar, W. Shyy, and R. Tran-Son-Tay, *Hydrodynamics of a compound drop with application to leukocyte modeling*, Phys. Fluid., **10**(4) (1998), 760–774.
- [6] H.C. Kan, W. Shyy, H.S. Udaykumar, P. Vigneron, and R. Tran-Son-Tay, *Effects of nuclei on leukocyte recovery*, Ann. Biomed. Eng., **27** (1999), 648–655.
- [7] R. Gautier, S. Laizet, and E. Lamballais, *A DNS study of jet control with microjets using an immersed boundary method*, Int. J. Comput. Fluid Dyn., **28** (2014), 393–410.
- [8] P. Ouro, L. Cea, L. Ramírez, and X. Nogueira, *An immersed boundary method for unstructured meshes in depth averaged shallow water models*, Int. J. Numer. M. Fluid., DOI: 10.1002/fld.4201, 2015.
- [9] C. Yan, W.X. Huang, G.W. Cui, C. Xu, and Z.S. Zhang, *A ghost-cell immersed boundary method for large eddy simulation of flows in complex geometries*, Int. J. Comput. Fluid Dyn., **29** (2015), 12–25.
- [10] H. Hua, J. Shin, and J. Kim, *Dynamics of a compound droplet in shear flow*, Int. J. Heat Fluid Fl., **50** (2014), 63–71.
- [11] Y. Kim, M.C. Lai, and C.S. Peskin, *Numerical simulations of two-dimensional foam by the immersed boundary method*, J. Comput. Phys., **229**(13) (2010) 5194–5207.
- [12] Y. Kim and Y. Seol, *Numerical simulations of two-dimensional wet foam by the immersed boundary method*, Comput. Struct., **122** (201), 259–269.
- [13] Y. Kim, M.C. Lai, C.S. Peskin, and Y. Seol, *Numerical simulations of three-dimensional foam by the immersed boundary method*, J. Comput. Phys., **269** (2014), 1–21.
- [14] S. Osher and J.A. Sethian, *Fronts propagating with curvature dependent speed: algorithms based on Hamilton–Jacobi formulations*, J. Comput. Phys., **79**(1) (1988), 12–49.
- [15] S. Osher and R.P. Fedkiw RP, *Level Set Methods and Dynamic Implicit Surfaces*. Springer-Verlag, New York, 2003.
- [16] F. Raees, D.R. Heul, and C. Vuik, *A mass-conserving level-set method for simulation of multiphase flow in geometrically complicated domains*, Int. J. Numer. M. Fluid, DOI: 10.1002/fld.4188, 2005.
- [17] J.A. Sethian and P. Smereka, *Level set methods for fluid interfaces*, Ann. Rev. Fluid Mech., **35** (2003), 341–372.
- [18] B. Merriman, J.K. Bence, and S. Osher, *Motion of multiple junctions a level set approach*, J. Comput. Phys., **12**(2) (1994), 334–363.
- [19] K.A. Smith, F.J. Solis, and D.L. Chopp, *A projection method for motion of triple junctions by level sets*, Interface. Free Bound., **4** (2002) 263–276.
- [20] S. Aland and F. Chen, *An efficient and energy stable scheme for a phase-field model for the moving contact line problem*, Int. J. Numer. M. Fluid., DOI: 10.1002/fld.4200, 2015.
- [21] J.W. Cahn and J.E. Hilliard, *Free energy of a nonuniform system. I. interfacial free energy*, J. Chem. Phys. **28**(2) (1958), 258–267.
- [22] D. Anderson, G.B. McFadden, and A.A. Wheeler, *Diffuse interface methods in fluid mechanics*, Ann. Rev. Fluid Mech., **30**(1) (1998) 139–165.

- [23] D. de Fontaine, *A computer simulation of the evolution of coherent composition variations in solid solutions*, Ph.D. Thesis, Northwestern University, USA, 1967.
- [24] D. Eyre, *Systems of Cahn–Hilliard equations*, SIAM J. Appl. Math., **53** (1993), 1686–1712.
- [25] J.F. Blowey, M. Copetti, and C.M. Elliott, *Numerical analysis of a model for phase separation of a multi-component alloy*, IMA J. Numer. Anal. **16** (1996), 111–139.
- [26] F. Boyer, C. Lapuerta, S. Minjeaud, B. Piar, and M. Quintard, *Cahn–Hilliard/Navier–Stokes model for the simulation of three-phase flows*, Transport Porous Med., **82**(3) (2010), 463–483.
- [27] M. Copetti, *Numerical experiments of phase separation in ternary mixtures*, Math. Comput. Simul. **52**(1) (2000), 41–51.
- [28] J.S. Kim, *Phase field computations for ternary fluid flows*, Comput. M. Appl. Mech. Eng., **196** (2007), 4779–4788.
- [29] J.S. Kim, *Phase-field models for multi-component fluid flow* Commun. Comput. Phys. **12** (2012) 613–661.
- [30] H.G. Lee and J. Kim, *Two-dimensional Kelvin–Helmholtz instabilities of multi-component fluids*, Euro. J. Mech. B-Fluid., **49** (2015), 77–88.
- [31] T.Y. Hou, Z. Li, S. Osher, and H. Zhao, *A hybrid method for moving interface problems with application to the Hele–Shaw flow*, J. Comput. Phys. **132**(2) (1997), 236–252.
- [32] F. Losasso, T. Shinar, A. Selle, and R. Fedkiw, *Multiple interacting liquids*, ACM T. Graphic., **25**(3) (2006), 812–819.
- [33] T. Oda, N. Satofuka, and H. Nishida, *Numerical analysis of particle behavior penetrating into liquid by level set method*, in: S.W. Armfield, P. Morgan (Eds.), Computational Fluid Dynamics 2002, Springer, Berlin Heidelberg, 2003, pp. 529–534.
- [34] K.A. Smith, F.J. Solis, L. Tao, K. Thornton, and M.O. De La Cruz, *Domain growth in ternary fluids: a level set approach*, Phys. Rev. Lett., **84** (2000), 91–94.
- [35] J.S. Kim and J. Lowengrub, *Phase field modeling and simulation of three-phase flows*, Interface. Free Bound., **7** (2005), 435–466.
- [36] M. Sussman, P. Smereka, and S. Osher, *A level set approach for computing solutions to incompressible two-phase flow*, J. Comput. Phys., **114**(1) (1994), 146–159.
- [37] H.G. Lee and J. Kim, *A second-order accurate non-linear difference scheme for the  $N$ -component Cahn–Hilliard system*, Physica A, **387**(19) (2008), 4787–4799.
- [38] D. Jacqmin, *Contact-line dynamics of a diffuse fluid interface*, J. Fluid Mech., **402** (2000), 57–88.
- [39] H. Hua, J. Shin, and J. Kim, *Level set, phase-field, and immersed boundary methods for two-phase fluid flows*, J. Fluid. Eng., **136** (2014), 021301.
- [40] J.U. Brackbill, D.B. Kothe, and C. Zemach, *A continuum method for modelling surface tension*, J. Comput. Phys., **100**(2) (1992), 335–354.
- [41] Y. Li, A. Yun, and J. Kim, *An immersed boundary method for simulating a single axisymmetric cell growth and division*, J. Math. Bio., **65**(4) (2012), 653–675.
- [42] F. Boyer and C. Lapuerta, *Study of a three component Cahn–Hilliard flow model*, ESAIM-Math. Model. Numer. Anal., **40**(4) (2006), 653–687.

- [43] A.J. Chorin, *Numerical solution of the Navier–Stokes equations*, Math. Comput., 22(104) (1968), 745–762.
- [44] Y. Li, A. Yun, D. Lee, J. Shin, D. Jeong, and J. Kim, *Three-dimensional Volume-conserving immersed boundary model for two-phase fluid flows*, Compu. Meth. Appl. Mech. Eng., 257 (2013), 36–46.
- [45] H. Hua, Y. Li, J. Shin, H. Song, and J. Kim, *Effect of confinement on droplet deformation in shear flow*, Int. J. Comput. Fluid Dyn., 27 (2013), 317–331.
- [46] C.W. Shu, *Essentially non-oscillatory and weighted essentially non-oscillatory schemes for hyperbolic conservation laws*, Springer, Berlin Heidelberg, 1998.
- [47] H.G. Lee, J.W. Choi, and J. Kim, *A practically unconditionally gradient stable scheme for the  $N$ -component Cahn–Hilliard system*, Physica A, 391 (2012), 1009–1019.
- [48] J.J. Eggleston, G.B. McFadden, and P.W. Voorhees, *A phase-field model for highly anisotropic interfacial energy*, Physica D, 150 (2001), 91–103.
- [49] J. Kim, S. Lee, and Y. Choi, *A conservative Allen–Cahn equation with a space-time dependent Lagrange multiplier*, Int. J. Eng. Sci., 84 (2014), 11–17.